



Article

Pressure–Temperature Phase Diagram of Multiferroic $\text{TbFe}_{2.46}\text{Ga}_{0.54}(\text{BO}_3)_4$

Alexander Krylov ^{1,*}, Svetlana Krylova ¹, Irina Gudim ¹, Yuri Kitaev ², Elena Golovkina ³, Haibo Zhang ⁴ and Alexander Vtyurin ^{1,3}

¹ Kirensky Institute of Physics, Federal Research Center KSC SB RAS, 660036 Krasnoyarsk, Russia; slanky@iph.krasn.ru (S.K.); irinagudim@mail.ru (I.G.); vtyurin@iph.krasn.ru (A.V.)

² Ioffe Institute, Politeknicheskaya 26, 194021 St. Petersburg, Russia; yu.kitaev@mail.ru

³ Institute of Engineering Physics and Radio Electronics, Siberian Federal University, 660041 Krasnoyarsk, Russia; e.v.golovkina@mail.ru

⁴ State Key Laboratory of Material Processing and Die and Mould Technology, School of Materials Science and Engineering, Huazhong University of Science and Technology, Wuhan 430074, China; hbzhang@hust.edu.cn

* Correspondence: shusy@iph.krasn.ru

Abstract: The pressure–temperature phase diagram of the multiferroic $\text{TbFe}_{2.46}\text{Ga}_{0.54}(\text{BO}_3)_4$ was studied for hydrostatic pressures up to 7 GPa and simultaneously with temperatures up to 400 K by the Raman spectroscopy technique. The structural phase transition from the $R32$ phase to the $P3_121$ phase was determined by observing the condensation of soft modes and the appearance of new lines. An increase in pressure leads to an increase in the temperature of the structural phase transition. These phases are stable over the entire investigated temperature and pressure range. No other phases have been found.

Keywords: ferroborate; phase transitions; multiferroics; p–T phase diagram



Citation: Krylov, A.; Krylova, S.; Gudim, I.; Kitaev, Y.; Golovkina, E.; Zhang, H.B.; Vtyurin, A. Pressure–Temperature Phase Diagram of $\text{TbFe}_{2.46}\text{Ga}_{0.54}(\text{BO}_3)_4$. *Magnetochemistry* **2022**, *8*, 59. <https://doi.org/10.3390/magnetochemistry8060059>

Academic Editor: George Youssef

Received: 15 April 2022

Accepted: 9 May 2022

Published: 1 June 2022

Publisher's Note: MDPI stays neutral with regard to jurisdictional claims in published maps and institutional affiliations.



Copyright: © 2022 by the authors. Licensee MDPI, Basel, Switzerland. This article is an open access article distributed under the terms and conditions of the Creative Commons Attribution (CC BY) license (<https://creativecommons.org/licenses/by/4.0/>).

1. Introduction

Ferroborates crystals with rare-earth elements in the structure and similar to the natural mineral huntite are still considered as a budding materials for optoelectronic devices and applications [1]. Some of them demonstrate rather high magnetoelectric effects [2,3]. The applications can be optimized by full or partial replacement of ions of rare earth elements or iron atoms in the structure [4–9]. In particular, it was found that the temperature of the structural phase transition in the $\text{HoFe}_3(\text{BO}_3)_4$ crystal can shift significantly when Fe is replaced by Ga ions [9].

The growth of these crystals and their initial characterization are presented in several publications [7–9]. It turned out that their $R32$ phase is built of spiral chains of FeO_6 octahedra directed along the c -axis. The phase transition in terbium ferroborate from the structure with $R32$ symmetry to the $P3_121$ symmetry group structure was detected by the Raman spectroscopy techniques at 198 K [10]. Later, this temperature was refined by other methods up to 192 K [11–13].

The magnetic phase transition in the $\text{TbFe}_3(\text{BO}_3)_4$ crystal was observed at 40 K [7] and was studied by several methods [14,15]. It was found that the magnetic properties of a crystal are determined by the interaction between two magnetic sublattices of Fe and Tb ions. Antiferromagnetic ordering occurs in the Fe sublattice with the magnetic moments of the ions directed along the third-order axis. The interaction of these two sublattices leads to the same ordering of the Tb magnetic moments along one axis. In this crystal, one more spin-reorientation transition of the first order was discovered with $H_c = 35$ Oe at 4.2 K [11,12,16]. NMR studies of $\text{TbFe}_3(\text{BO}_3)_4$ revealed six nonequivalent magnetic sublattices of Fe ions [17]. Functional density modeling was performed for $\text{TbFe}_3(\text{BO}_3)_4$ [11,12], $\text{NdFe}_3(\text{BO}_3)_4$, $\text{NdGa}_3(\text{BO}_3)_4$ [18], $\text{HoGa}_3(\text{BO}_3)_4$ crystals [19].

The Raman spectroscopy technique has been repeatedly used to study structural and magnetic transitions in single crystals and ferrobates solid solutions ($\text{Ho,NdFe}_3(\text{BO}_3)_4$ [5,6], $\text{Ho(Fe,Ga)}_3(\text{BO}_3)_4$ [9], $\text{GdFe}_3(\text{BO}_3)_4$ [20], $(\text{Sm,L a})\text{Fe}_3(\text{BO}_3)_4$ [8], $\text{TbFe}_{2.5}\text{Ga}_{0.5}(\text{BO}_3)_4$ [21], $\text{SmFe}_3(\text{BO}_3)_4$ [22]. The temperature dependence of the Raman spectra in a pure $\text{TbFe}_3(\text{BO}_3)_4$ single crystal was studied early by optical spectroscopy [23], Raman spectroscopy [10,24], magnetodielectric and magnetoelastic coupling properties [25], and the Faraday effect [26]. Here, anomalies were found in the low-frequency range near the magnetic phase transition [10,24], as well as at medium frequencies near the structural phase transition [24,25].

The temperature structural phase transition was investigated by the method of Raman scattering also in the solid solution $\text{TbFe}_{2.5}\text{Ga}_{0.5}(\text{BO}_3)_4$ [21]. Experiments at high pressures were carried out in the $\text{HoFe}_3(\text{BO}_3)_4$ and $\text{TbFe}_3(\text{BO}_3)_4$ crystals [27,28]. In the same works, a phase diagram was obtained. Similar anomalies can be expected in the Raman spectra of other $\text{TbFe}_{3-x}\text{Ga}_x(\text{BO}_3)_4$ solutions [9].

The gallium is a non-magnetic atom. When iron atom is replaced by gallium atom, the effect of the magnetic iron sublattice on the magnetic terbium sublattice decreases. However, this requires a concentration of gallium so as not to break the symmetry of the host crystal. $\text{TbFe}_{2.46}\text{Ga}_{0.54}(\text{BO}_3)_4$ is one of the samples in the series from pure iron to supposed pure gallium, close to the phase existence limit.

Possible transitions in the $\text{TbFe}_{2.46}\text{Ga}_{0.54}(\text{BO}_3)_4$ solid solution with increasing pressure have not been studied. Among the possible external parameters, hydrostatic pressure has such specificity that it allows for changing the interatomic distances, and thus the interactions, to a much larger extent than any other parameter like temperature or magnetic field. In spite of many investigations with other thermodynamic parameters, a broad overview of the effect of hydrostatic pressure on rare-earth ferrobates is still lacking. Information about of the temperature-pressure phase diagram is important for materials applying for practical use. The purpose of this work is to study the p-T phase diagram in a crystal. For this purpose, we plan to carry out polarized Raman experiments at various angles, assign experimental modes to irreducible representations based on symmetry analysis, carry out studies with temperature and pressure changes, and construct a temperature–pressure phase diagram.

2. Materials and Methods

Single crystals of $\text{TbFe}_{2.46}\text{Ga}_{0.54}(\text{BO}_3)_4$ were grown from a solution-melt based on $(\text{Bi}_2\text{Mo}_3\text{O}_{12}\text{--B}_2\text{O}_3\text{--Tb}_2\text{O}_3)$. Solution-melts weighing $P = 150$ g were prepared in a platinum cylindrical crucible ($D = 40$ mm, $H = 50$ mm) by sequential fusion at $T = 1100$ °C of the oxides Bi_2O_3 , MoO_3 , B_2O_3 , Fe_2O_3 , Ga_2O_3 . At the stage of dissolution at the same temperature, the stirred solution-melt was kept for 8–10 h. This time is sufficient for its complete homogenization. The saturation temperature was determined with an accuracy of ± 2 °C using test crystals, which were preliminarily obtained on a rod crystal holder in the spontaneous nucleation mode.

After the final homogenization, the temperature of the solution-melt was reduced to $T = T_{\text{sat}} + 7$ °C (T_{sat} temperature of saturation), the rod with a seed was immersed in the solution-melt, and its reverse rotation was switched on at a rate of $\omega = 30$ rpm. After 10 h, the temperature was lowered to $T = T_{\text{sat}} - 10$ °C and then smoothly according to the program with an increasing rate $dT/dt = 1 - 3$ °C/day. The growth continued up to 14 days. During this time, high-quality crystals with sizes up to 4–12 mm grew. The crystal holder with the grown crystals was raised above the molten solution, and the furnace was cooled to room temperature with the power turned off.

Raman spectra were collected in backscattering geometry by Horiba Jobin-Yvon T64000 triple spectrometer (Horiba, France) operating in the dispersion subtraction mode. Resolution of the low-frequency region in the study of the soft mode was improved to 1.2 cm^{-1} . We used a Spectra-Physics Excelsior-532-300-CDRH (USA) 532 nm diode-pumped visible CW solid-state single-mode laser with a power of 5 mW on sample as a source of exciting

light. The samples were optically transparent unoriented greenish single crystals less than 3 mm in size with natural faceting and did not contain defects and inclusions visible under a microscope. The temperature of the structural phase transition was determined from the temperatures of the anomalies in the spectra, including the appearance of new lines in the Raman spectrum, and by analyzing the behavior of the soft modes. High-temperature gas membrane-driven diamond anvil cell (HT-DAC) device Diacell μ Scope DAC HT(G) type (EasyLab, Kent, UK) was used for Raman study of processes at simultaneously high pressure and temperature. The stainless steel gasket with an initial thickness of 250 μ m pre-indented to 80 μ m was used in the experiment. The pressure was monitored by the shift of the $^5D_0 - ^7F_0$ fluorescence band of Sm^{2+} ion in a small $\text{SrB}_4\text{O}_7\text{:Sm}^{2+}$ crystal placed in the sample's vicinity within the experimental error of about 0.05 GPa [29,30]. The experimental temperature was monitored using a type K thermocouple in contact with the gasket and diamond anvil. The most commonly used mixture 4:1 of methanol and ethanol alcohols has been used as a hydrostatic pressure transmission media.

3. Results and Discussion

3.1. Symmetry Analysis

The analysis of the structural transition of $\text{TbFe}_3(\text{BO}_3)_4$ using the Bilbao Crystallographic Server [31,32] showed that the phase transition is due to the instability of the $R32$ phase at Λ point of the Brillouin zone. Mode Λ_3 at Λ point of the Brillouin zone in $R32$ phase goes to mode Γ_1 with A_1 symmetry (soft mode) at the Γ point of the Brillouin zone in the $P3_121$ phase. The existence of a soft mode with an energy minimum at the Λ point in the Brillouin zone, at the critical temperature (192.5 K), was experimentally confirmed by inelastic neutron scattering [13].

In the high-temperature $R32$ phase of the $\text{TbFe}_3(\text{BO}_3)_4$ crystal, the representation of vibrations active in Raman scattering at the center of the Brillouin zone is

$$G_{\text{Ram}}(R32) = 7A_1 + 19E \quad (1)$$

At the center of the Brillouin zone, the vibrational representation active in Raman scattering for the $P3_121$ phase can be decomposed as

$$G_{\text{Ram}}(P3_121) = 27A_1 + 59E \quad (2)$$

An unoriented sample is used in the experiment at high hydrostatic pressures. This is due to the microscopic dimensions of the sample—usually, the size does not exceed 70–100 μ m. Through the analysis in a laboratory coordinate system that differs from the crystallographic one by rotations to Euler's angles, the following transformations can be performed.

The relative Raman modes intensity can be presented by:

$$I \propto |e_i R e_s|^2 \quad (3)$$

where I is the scattered Raman intensity; R is the Raman tensor, e_i and e_s represent the polarized unit vectors of the incident and scattered lights [33–35]. The Raman tensors R depend on the D_3 point group for both space groups [36]. The Raman tensor components for the $R32$ (No. 155) and $P3_121$ (No. 155) space groups in which the corresponding vibrations are active are presented in Table 1, where a , b , c , d represent the Raman tensors element.

Table 1. Raman tensors for the D_3 (32) point group.

A_1			$E(x)$			$E(y)$		
a	0	0	c	0	0	0	$-c$	$-d$
0	a	0	0	$-c$	d	$-c$	0	0
0	0	b	0	d	0	$-d$	0	0

The e_i and e_s in parallel configuration in Cartesian coordinates can be defined as

$$e_i = (0, 1, 0) \quad (4)$$

$$e_s = (0, 1, 0) \quad (5)$$

The e_s in cross configuration in Cartesian coordinates can be defined as

$$e_s = (1, 0, 0) \quad (6)$$

Considering the Euler matrix, Φ_{xyz} (and its inverse $\tilde{\Phi}_{xyz}$) and presented in Appendix A as (A1), which transforms the crystal coordinates into the experimental ones, the Raman tensor is given by:

$$R_{xyz} = \Phi_{xyz} R \tilde{\Phi}_{xyz} \quad (7)$$

The calculated by formula (3) Raman modes are presented in Figures A1–A3. The rotation angle intensity map of calculated Raman modes in HH and HV polarisation is presented in Figure A4.

The $\text{TbFe}_3(\text{BO}_3)_4$ crystal includes two magnetic subsystems of Fe and Tb ions. The analysis of the magnetic ordering in the crystal showed that the magnetic transition in the low-temperature $P3_121$ phase is possible from paramagnetic $P3_1211'$ phase (152.2.1264) phase to probable $P_{2c}3_221$ (152.4.1266) antiferromagnetic phase. Notations correspond to [37–39]. In the experimental work [11], it is assumed that the magnetic transition occurs in the P_c3_221 (154.44) phase in Belov–Neronova–Smirnova notation [40,41]. It is the same $P_{2c}3_221$ (152.4.1266) phase as we find using the Bilbao Crystallographic Server but in Opechowski–Guccione notation [39].

One can assume some changes will occur in the spectra of $\text{TbFe}_3(\text{BO}_3)_4$ crystal when some of the Fe ions will be replaced by Ga ions. We expect a shift in the structural phase transition temperature, a shift in the temperature of the magnetic ordering, and small changes in line positions. For example, in the work [9], it is shown that the temperature of the structural phase transition at atmospheric pressure in $\text{HoFe}_{3-x}\text{Ga}_x(\text{BO}_3)_4$ crystals decreases with an increase in the concentration of gallium. We suggest that the proximity of the structural and magnetic transitions in this crystal can cause a strong interaction of the structural and magnetic order parameters.

3.2. Angular-Dependent Raman Spectra

The angular dependencies of the Raman spectra were measured for an unoriented piece of a single crystal. This was done for two reasons. First, in the Raman spectra of an unoriented crystal, all lines of the spectrum are present; in certain components of the scattering tensor, some lines can be forbidden by the selection rules. The presence of all possible lines in the spectrum simplifies the detection of anomalies associated with structural and magnetic transitions. Second, in experiments under high hydrostatic pressures, the orientation is difficult to control. Even a correctly placed sample can turn into a position during the pressurization process, the spectra of which will be the same as those of non-oriented samples. The angular dependencies of the intensities of the spectral lines were analyzed according to the theoretical dependencies presented in the appendix. Lines with different types of symmetry give different patterns. Theoretically calculated patterns for various angles are shown in Figures A1–A3. The performed assignment by vibration types together with the experimentally obtained patterns is presented in Table 2.

Table 2. Dependence of the peak position of the vibrational mode on the angle of rotation. Back scattering geometry at 296 K (*R*32 phase) in TbFe_{2.46}Ga_{0.54}(BO₃)₄ crystal.

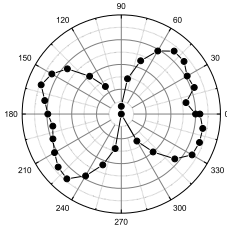
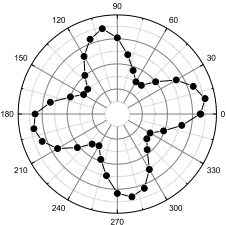
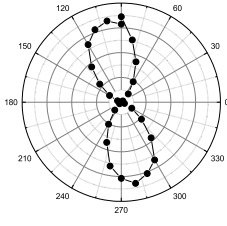
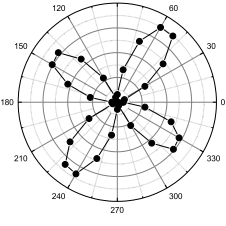
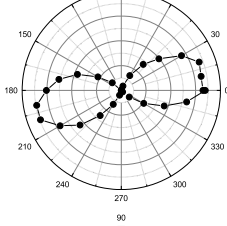
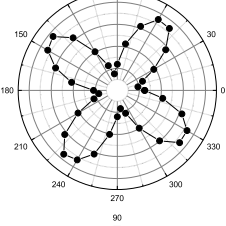
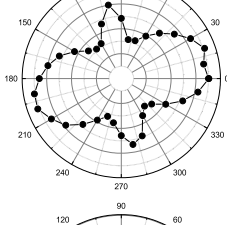
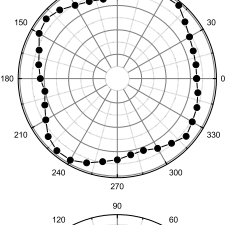
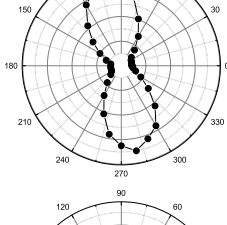
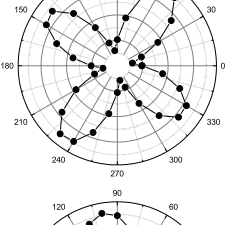
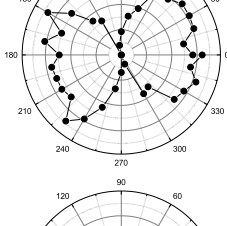
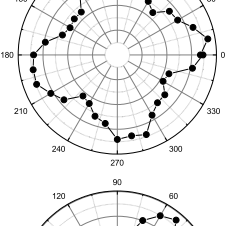
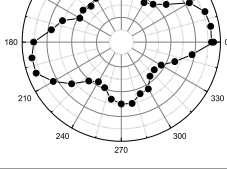
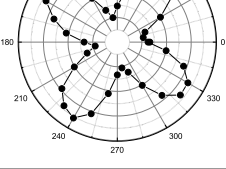
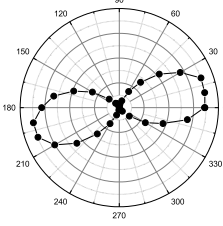
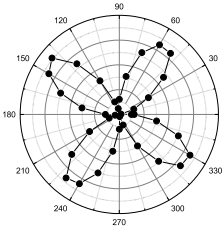
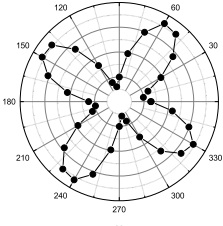
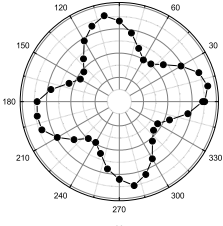
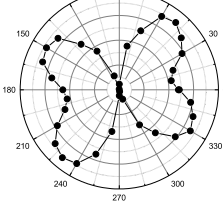
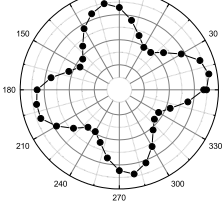
Raman Shift, cm ^{−1}	HH	HV	Irred. Repres.
93			E
181			A ₁
199			A ₁
448			E
482			A ₁
736			E
961			E

Table 2. Cont.

Raman Shift, cm^{-1}	HH	HV	Irred. Repres.
991			A_1
1237			E
1413			E

The low-frequency modes ($93, 181 \text{ cm}^{-1}$) are due to lattice vibrations and displacement of heavy atoms of Tb. The $200\text{--}250 \text{ cm}^{-1}$ modes are attributed to the vibrations of the BO_3 triangles and the displacements of the iron atoms. The region from 400 to 500 cm^{-1} is attributed with bending of BO_3 triangles and oxygen displacements in FeO_6 octahedra. The range $600\text{--}750 \text{ cm}^{-1}$ includes modes of bending of BO_3 triangles and oxygen atoms' vibrations in FeO_6 octahedra, TbO_6 prisms. The region of $950\text{--}1000 \text{ cm}^{-1}$ includes the displacements of the vertices of the planar BO_3 triangles and the shifts of oxygen atoms in the FeO_6 octahedra. The vibration modes in the region of about $1200\text{--}1300 \text{ cm}^{-1}$ are associated with the stretching of the B–O bond inside the BO_3 triangles [10,24,28].

3.3. Phase Transitions at Atmospheric Pressure

The temperature dependence of Raman spectra of $\text{TbFe}_{2.46}\text{Ga}_{0.54}(\text{BO}_3)_4$ crystal were studied in the temperature range from 8 to 400 K. The full Raman spectra of $\text{TbFe}_{2.46}\text{Ga}_{0.54}(\text{BO}_3)_4$ at some temperatures are shown in Figure 1. The concentration of gallium is not enough to change the $R32$ symmetry of the crystal under normal conditions. If the symmetry of the crystal were to change, we would see changes in the spectrum associated with the change in symmetry compared to previously published spectra of the $\text{TbFe}_3(\text{BO}_3)_4$ crystal [10,24,25].

The appearance of new bands with decreasing temperature has been observed in the region of about 1000 cm^{-1} , 390 cm^{-1} and lowest wavenumber (soft mode) as it was predicted according to group-theoretical analysis for isostructural materials [9,29].

Raman spectra transformation with temperature of $\text{TbFe}_{2.46}\text{Ga}_{0.54}(\text{BO}_3)_4$ in the mid-wavenumber region is presented in Figure 2. The appearance of new lines at 374 and 276 cm^{-1} have been observed (Figure 2). The presence of these lines in the spectra can be an indicator of belonging to a phase with $P3_121$ symmetry and the absence of lines indicating belonging to the $R32$ symmetry phase.

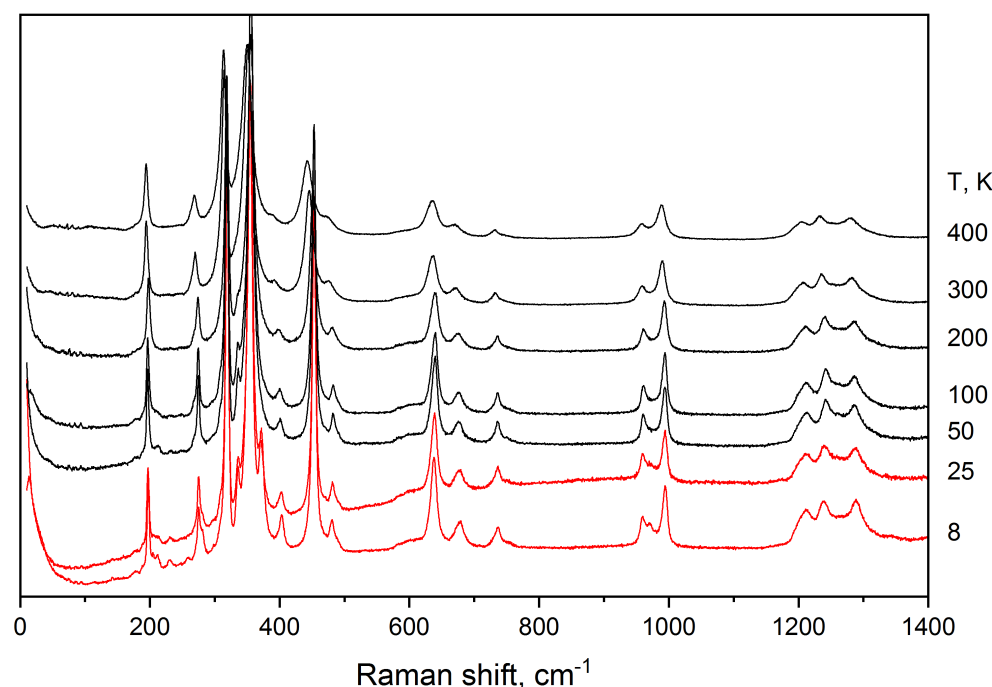


Figure 1. Full Raman spectra transformation with temperature of $\text{TbFe}_{2.46}\text{Ga}_{0.54}(\text{BO}_3)_4$. Color code: black— $R32$ phase, red— $P3_121$ phase.

An article was previously published about “soft” (low-frequency) temperature modes in this crystal [42]. Therefore, we did not consider them in this work. We found some anomalies in the behavior of the hard modes below 50 K. Hard modes are optically active phonons which show systematic changes of their Raman spectra when the structural properties of a material are changed—heating or application of pressure. This feature is a great advantage for the analysis of materials. The relative changes of the phonon frequencies are usually below several percent of their total energies, which is why “hard modes” instead of “soft modes” [43,44]. New modes at 370 and 970 cm^{-1} appear close to 33 K (Figures 1 and 2). The splitting hard mode peaks are attributed to the structural phase transition [45,46]. The new modes appear according to the selection rules. In Figure 3, one can see the dependence of the ratio of the integral intensities of several pairs of hard modes on the temperature. The slope of the curve of this dependence sharply changes near 33 K. This behavior is characteristic of a structural phase transition. It is the fine manifestation of fluctuations of the structural order parameter at low temperatures. An additional break is visible at a temperature of about 50 K. It is clearly seen from the deviation from the dependence at high temperatures, the approximation of which is indicated by a dotted line. We attribute this behavior to the transition of magnetic ordering.

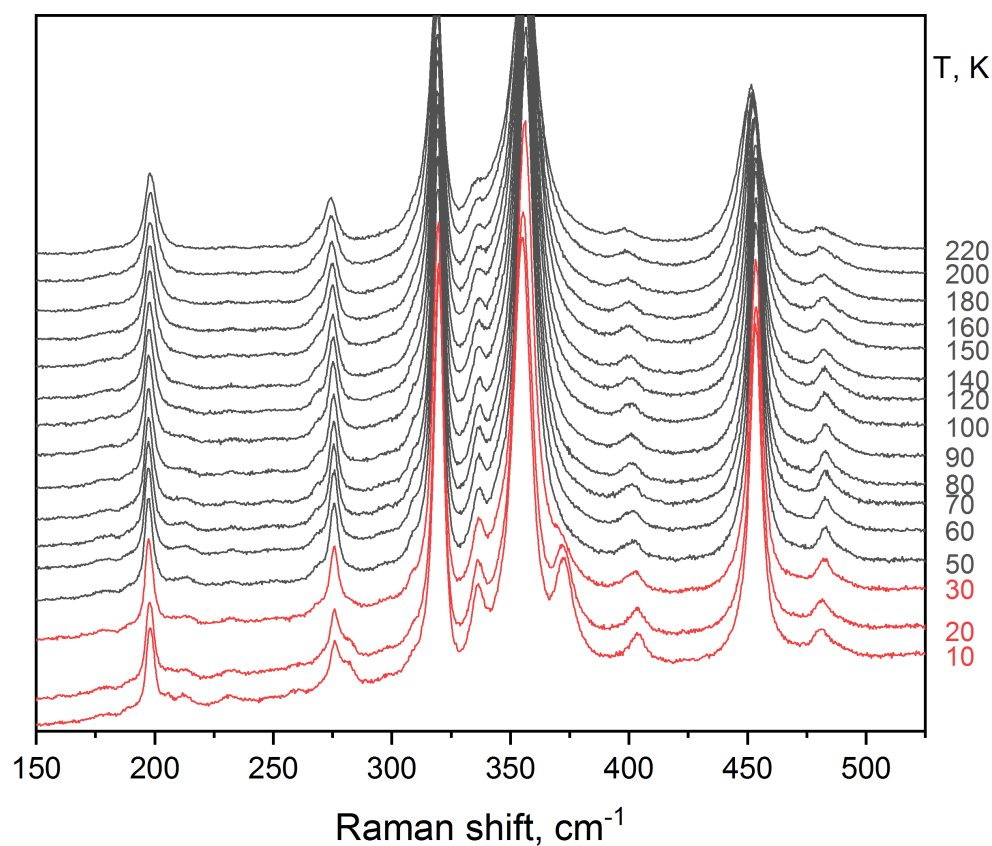


Figure 2. Raman spectra transformation with temperature of $\text{TbFe}_{2.46}\text{Ga}_{0.54}(\text{BO}_3)_4$ in the mid-wavenumber region. Color code: black—R32 phase, red— $P3_121$ phase.

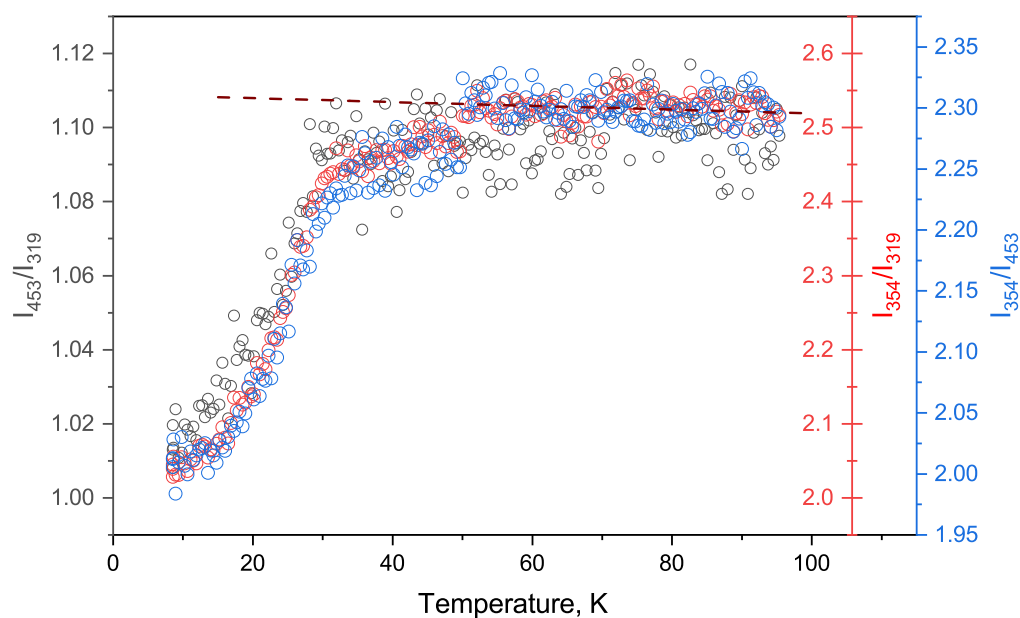


Figure 3. The relation of the integral intensities of several strongest hard modes.

The crystal $\text{TbFe}_{2.46}\text{Ga}_{0.54}(\text{BO}_3)_4$ undergoes a structural phase transition at $T_c = 33$ K. The temperature of the structural phase transition is close to the magnetic ordering temperature. The changes observed in the spectra point to the structural ordering arising.

Temperature dependence of 273 cm^{-1} internal mode position is given in Figure 4a. Width of this line reveals some transitional effects as well. The temperature dependencies of the 319 cm^{-1} line position and its width is given in Figure 4b. The slope of the 319 cm^{-1} line

position dependence changes below the transition temperature Figure 4b. Figure 4c shows temperature dependence of the 356 cm^{-1} internal mode. A small additional shift of the line width appears in a narrow (about 0.4 K) region below 40 K . The shift decreases in the $R32$ phase under cooling, then sharply changes the direction in the second phase. Temperature dependencies of 480 cm^{-1} (A_1) line position and width are shown in Figure 4d. After the transition point (33 K), line position goes down with cooling. The temperature of transition is shown by the dashed lines in Figure 4. Temperature dependencies of the 637 cm^{-1} line position and the width are given in Figure 4e. Positions of the 674 cm^{-1} line and width change slightly under cooling (Figure 4f).

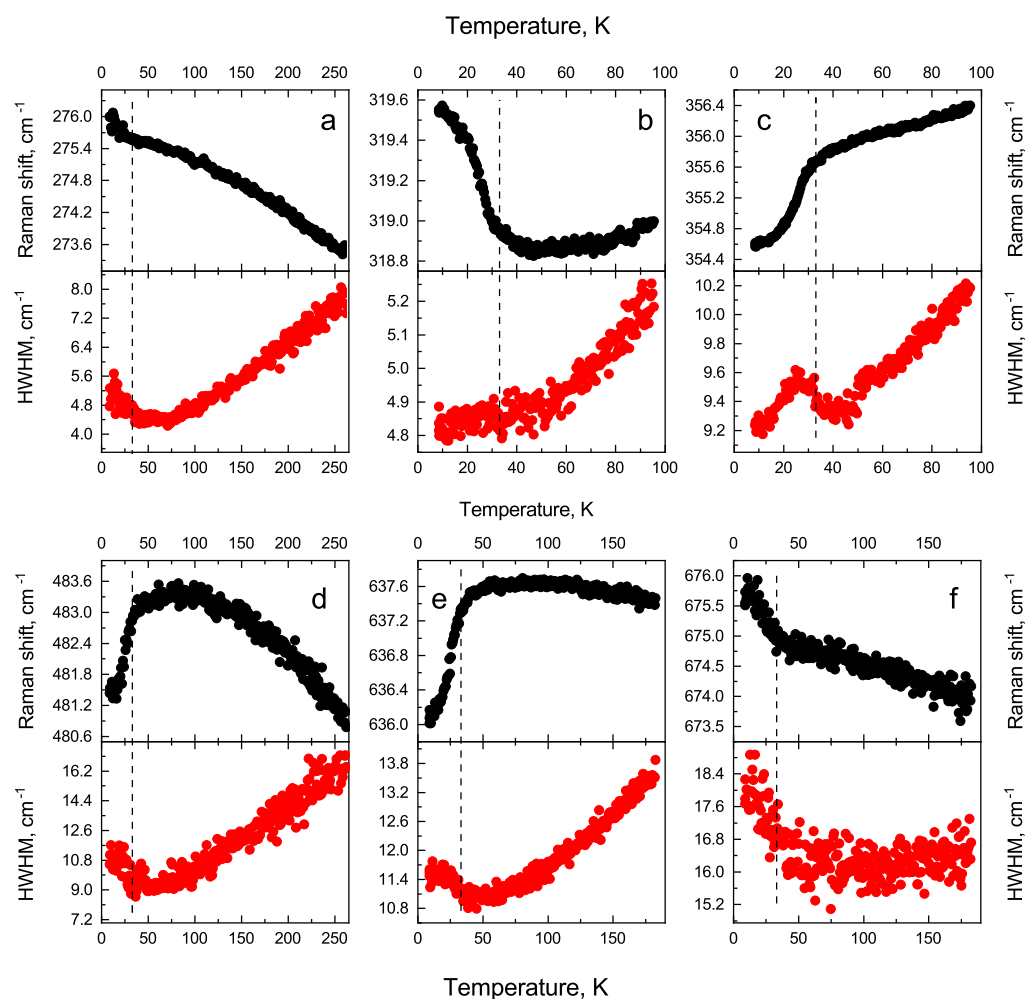


Figure 4. (a–f) Temperature dependencies of Raman line positions (black color) and halfwidths (red color). The dashed line denotes the temperature of structural phase transition 33 K .

3.4. p – T Phase Diagram

Thermocouple in contact with the gasket measures the experimental temperature within the diamond anvil cell. Sample temperature could differ from the values given from the thermocouple. We performed experiments with two pressure sensors for calibrating thermocouple reading. We used a small $\text{SrB}_4\text{O}_7\text{:Sm}^{2+}$ crystal as a pressure sensor independent from the temperature and the ruby chip as a sensor reading which depends both on the pressure and the temperature [47,48]. With the shift of the ruby luminescence band, consisting of independent contributions of temperature and pressure, and using the reading of the second sensor as pressure data, we could calculate the temperature inside the pressure chamber. We got a calibration curve for temperature correction comparing the thermocouple data and the calculated ones. The temperature correction method is described in detail in the article [27].

All changes of the Raman spectrum of the $\text{TbFe}_{2.46}\text{Ga}_{0.54}(\text{BO}_3)_4$ crystal at the temperature of phase transition point are well known and described early. Raman spectra transformation with pressure and constant ambient temperatures are presented in Figure 5. The phase transition point could be determined by analyzing the sequence of Raman spectra acquired during sample temperature changes at quasi constant pressure by varying the temperature of the resistive DAC heater. During the experiment, we set up some pressure value and then incrementally vary solely the temperature; consequently, the pressure in the DAC chamber slightly increases because of liquid media volume expansion with temperature increment. Spectral features indicate what the phase transition occurred: first, feature is a soft-mode condensation accompanying the structural phase transition in low-wavenumber region of Raman spectra sequence. Second, features have new lines appearing in the middle and high wavenumber regions, all of them corresponding to vibration of BO_3 groups. All experimental pressure–temperature points after the analysis mentioned above, according to the assignment to one of phases, are presented in Figure 6. Points belonging to the phase R32 are located lower on the pressure scale, whereas phase P_{3121} spread far to the right on the pressure scale to the high-pressure region. Acquired Raman spectra for any thermodynamical parameters (temperature and pressure) could be assigned to phase R32, or to the phase P_{3121} , or to the phase boundary. There were no spectra found that do not meet any of the phases mentioned previously and possibly belong to the new high-pressure high-temperature phase.

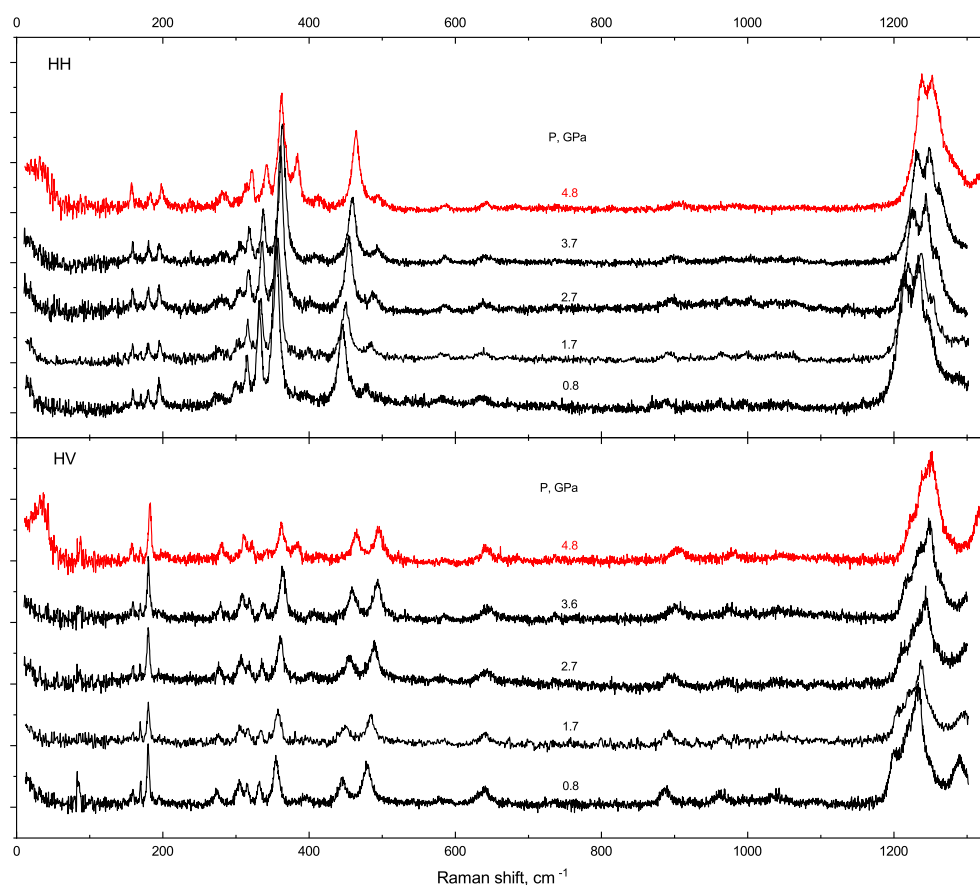


Figure 5. Raman spectra transformation with pressure of $\text{TbFe}_{2.46}\text{Ga}_{0.54}(\text{BO}_3)_4$ at 296 K. Color code: black—R32 phase, red— P_{3121} phase.

The p – T phase diagram of the $\text{TbFe}_3(\text{BO}_3)_4$ crystal after applying temperature correction is presented in Figure 6. The temperatures of structural transition increase with pressure, and the dependencies $T(p)$ of the boundary between the R32 phase and P_{3121} phase are described by linear equation $T(p) = a + bp$, where $a = 32.53 \pm 4.11$ K and

$b = 57.31 \pm 0.833 \text{ K} \cdot \text{GPa}^{-1}$. Therefore, the temperature ranges of the $P3_121$ phases increase under pressure. No triple points were revealed in the phase diagram. Photos of the sample crystal in the DAC at several $p - T$ conditions are presented in Figure A5.

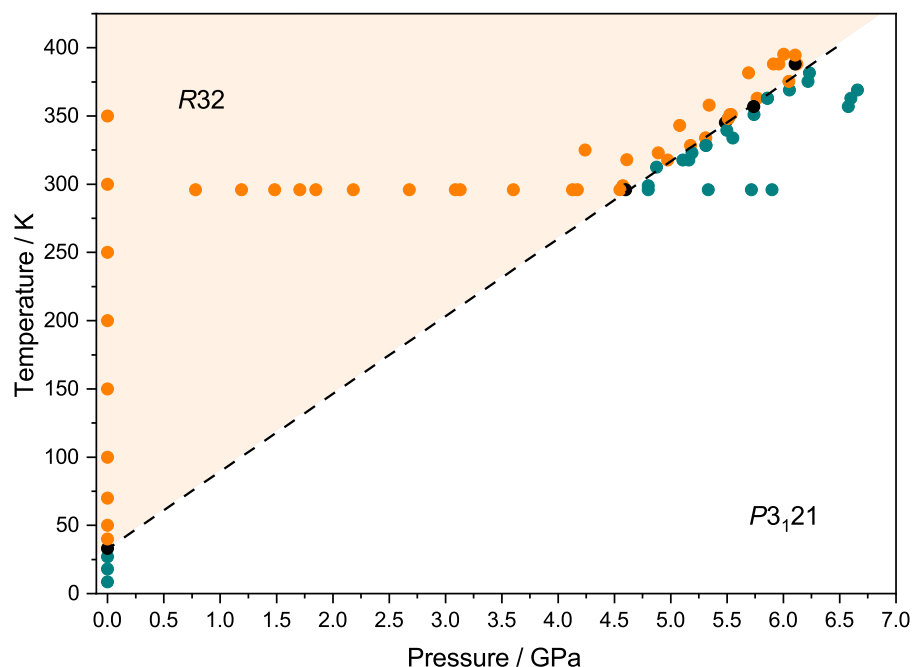


Figure 6. p – T phase diagram of $\text{TbFe}_{2.46}\text{Ga}_{0.54}(\text{BO}_3)_4$ crystal. Color code: orange—phase $R32$, dark cyan—phase $P3_121$, black—phase boundary.

4. Conclusions

The experimental study of the angular dependencies of the mode intensity of the Raman scattering spectra made it possible to determine the types of vibrations and interpret the spectra. The crystal $\text{TbFe}_{2.46}\text{Ga}_{0.54}(\text{BO}_3)_4$ undergoes a structural phase transition from the $R32$ phase to the $P3_121$ phase at $T_1 = 33 \text{ K}$, and the transition is accompanied by soft modes restoration and condensation. The temperature of the structural phase transition is close to the likeliest magnetic ordering temperature. The changes in the spectra are observed in the low-wavenumber region (up to 300 cm^{-1}) and the middle part of the spectra (up to 1100 cm^{-1}): the modes related to structural ordering arise. We suggest that the proximity of the structural and magnetic transitions in this crystal can cause a strong interaction of the structural and magnetic order parameters. Theoretical angular dependencies of the intensities of lines of various symmetries are obtained. The assignment of the experimental lines of the Raman spectrum according to the types of vibrations is made based on an analysis of theoretical dependencies.

The internal magnetic field leads to magnetic ordering of the sublattices of the sample, which respectively affect the behavior of the crystal phonon modes in the low-temperature region. Peculiarities of the Raman spectra manifested in anomalous shifts in the positions of the lines in the spectrum indicating the magnetic ordering in crystal were detected. The temperature of the magnetic ordering was estimated as $T_n = 50 \text{ K}$.

The Raman spectroscopy study of the $\text{TbFe}_{2.46}\text{Ga}_{0.54}(\text{BO}_3)_4$ crystal has been performed in the methanol–ethanol alcohol medium at simultaneously high pressure and temperature (up to 6.7 GPa and 390 K). The pressure–temperature phase diagram has been obtained up to pressure–temperature conditions, causing destruction of the sample. The phase boundary equation was obtained, and it remains linear at all investigated pressures and temperature ranges.

Author Contributions: Conceptualization, A.K.; methodology, A.K. and I.G.; software, E.G. and A.K.; formal analysis, S.K. and Y.K.; investigation, A.K. and E.G.; writing—original draft preparation, A.K., S.K., I.G., Y.K., E.G. and H.Z.; writing—review and editing, H.Z. and A.V.; visualization, A.K., E.G. and S.K.; supervision, A.V. All authors have read and agreed to the published version of the manuscript.

Funding: The research of Krylov A. and Gudim I. was funded by RFBR, Krasnoyarsk Territory and Krasnoyarsk Regional Fund of Science, project number 20-42-240009. This work of Vtyurin A., Krylova S. was financially supported by the Russian Foundation for Basic Research and DFG (Deutsche Forschungsgemeinschaft) project number No 21-52-12018.

Institutional Review Board Statement: Not applicable.

Informed Consent Statement: Not applicable.

Data Availability Statement: The data presented in this study are available on request from the corresponding author.

Acknowledgments: The experiments were performed in the Krasnoyarsk Regional Center of Research Equipment of Federal Research Center “Krasnoyarsk Science Center SB RAS”.

Conflicts of Interest: The authors declare no conflict of interest. The funders had no role in the design of the study; in the collection, analyses, or interpretation of data; in the writing of the manuscript, or in the decision to publish the results.

Abbreviations

The following abbreviations are used in this manuscript:

MDPI	Multidisciplinary Digital Publishing Institute
FWHM	Full width at half maximum
HH	Parallel polarisation of incident and scattered light
HV	Cross polarisation of incident and scattered light

Appendix A. Calculated Intensities of Raman Modes

The calculation of Raman intensity has been done by formula (3). The Raman tensor parameters a, b, c, d were taken as equal to 1. The calculated modes are presented in Figures A1–A3. Figure A1 was made for an angle of 30 degrees with the z-axis. Figure A2 shows the intensities of the Raman modes for an angle of 60 degrees with the z-axis. In Figure A3, the angle with the z-axis is 90 degrees.

In order to find the intensity of the Raman mode at any angle, intensity maps were obtained for each of the three Raman modes in two polarizations. The rotation angle intensity map of calculated Raman modes in HH and HV polarisation is presented in Figure A4.

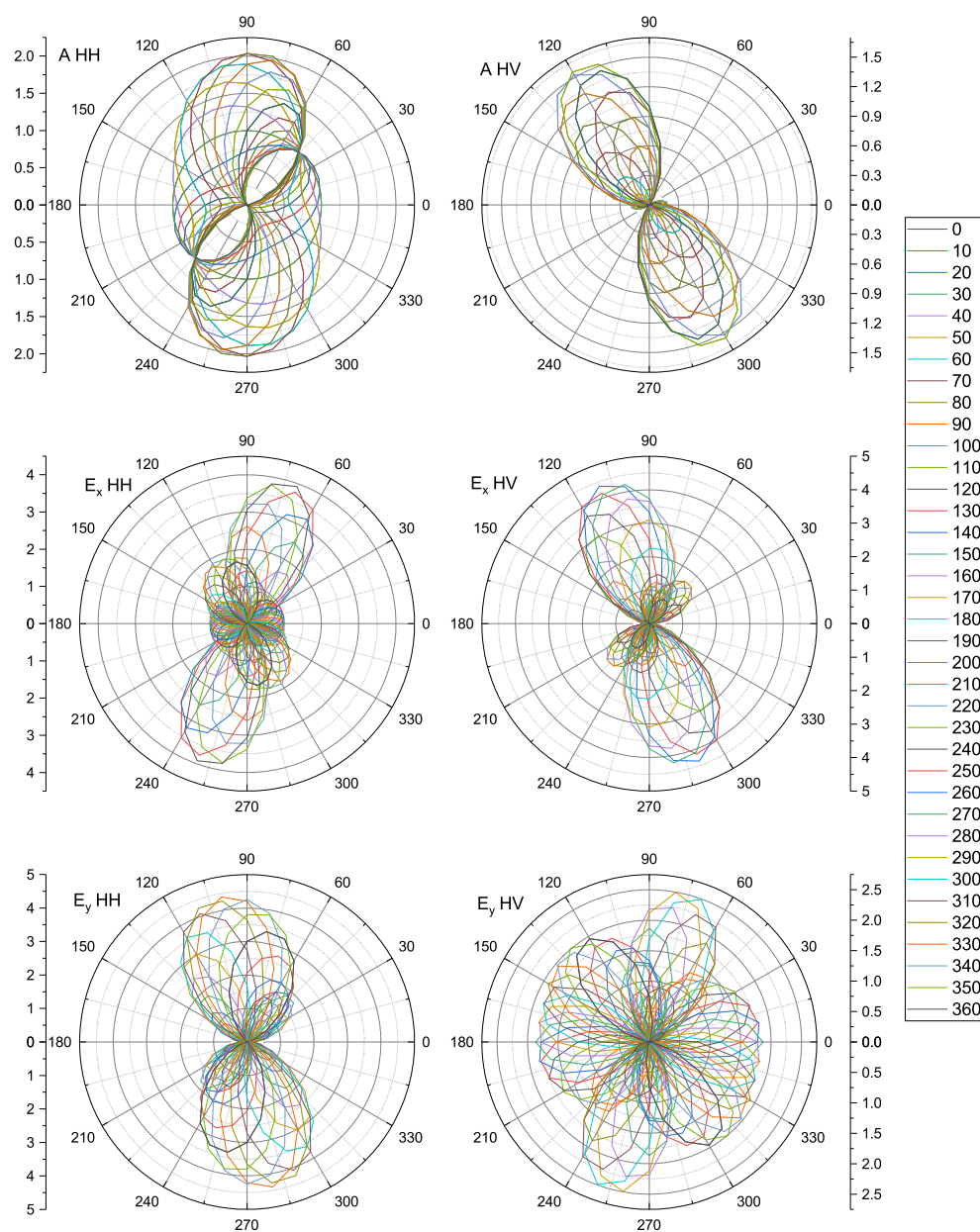


Figure A1. Calculated intensity dependence of Raman modes in the HH and HV polarisation on rotation angle in plane. The angle to z-axis is 30 degrees.

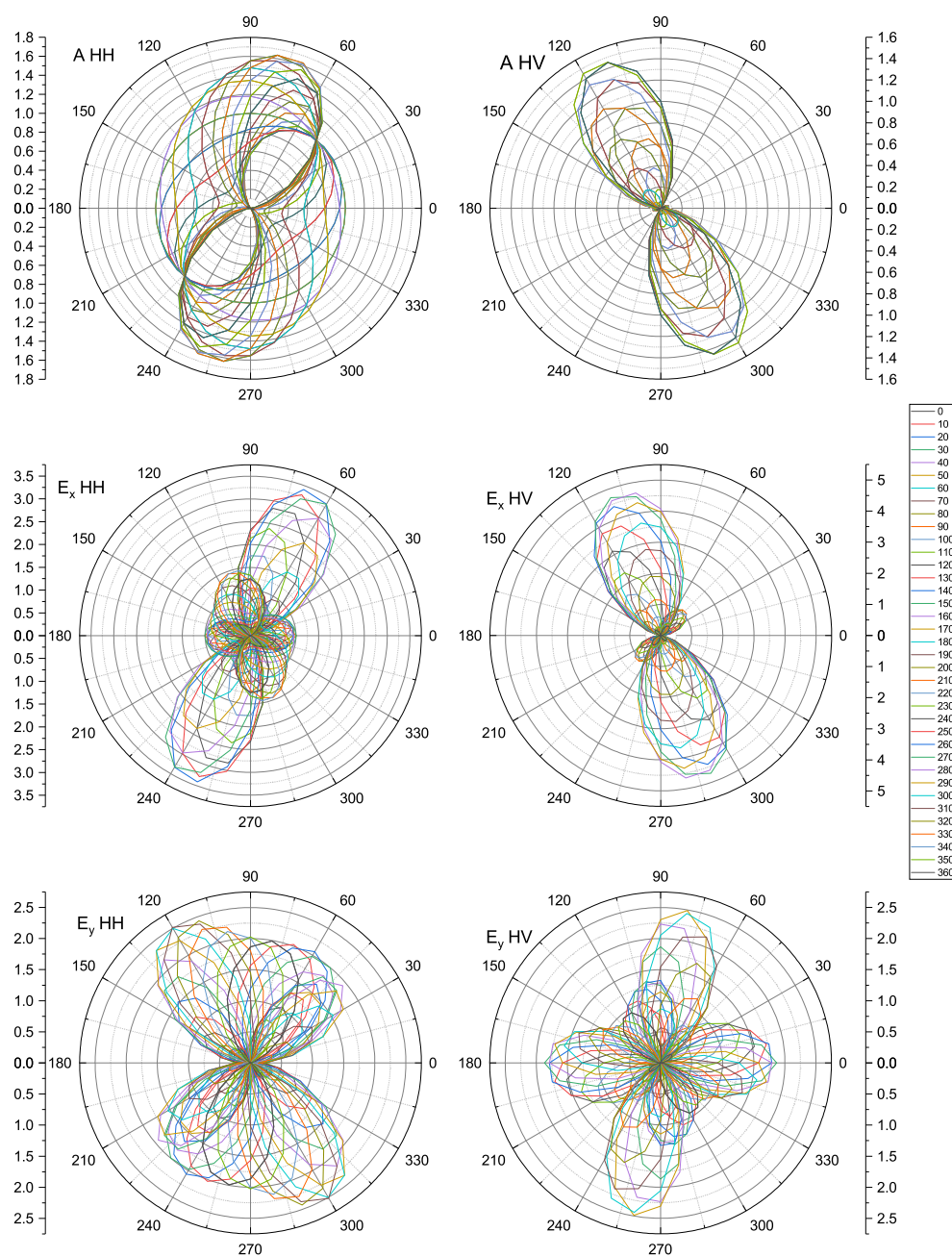


Figure A2. Calculated intensity dependence of Raman modes in the HH and HV polarisation on rotation angle in the plane. The angle to z-axis (vertical) is 60 degrees.

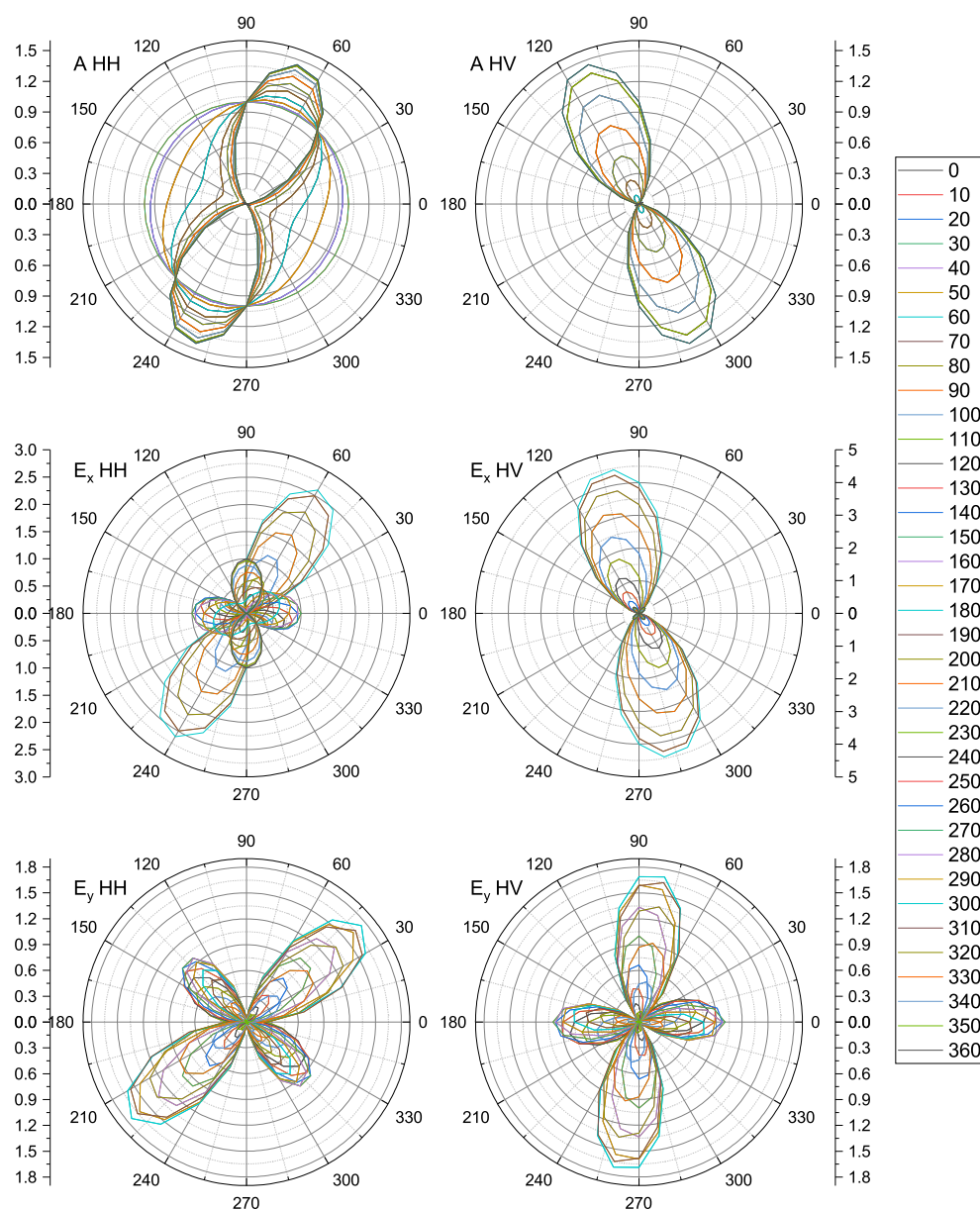


Figure A3. Calculated intensity dependence of Raman modes in the HH and HV polarisation on rotation angle in plane. The angle to z-axis is 90 degrees.

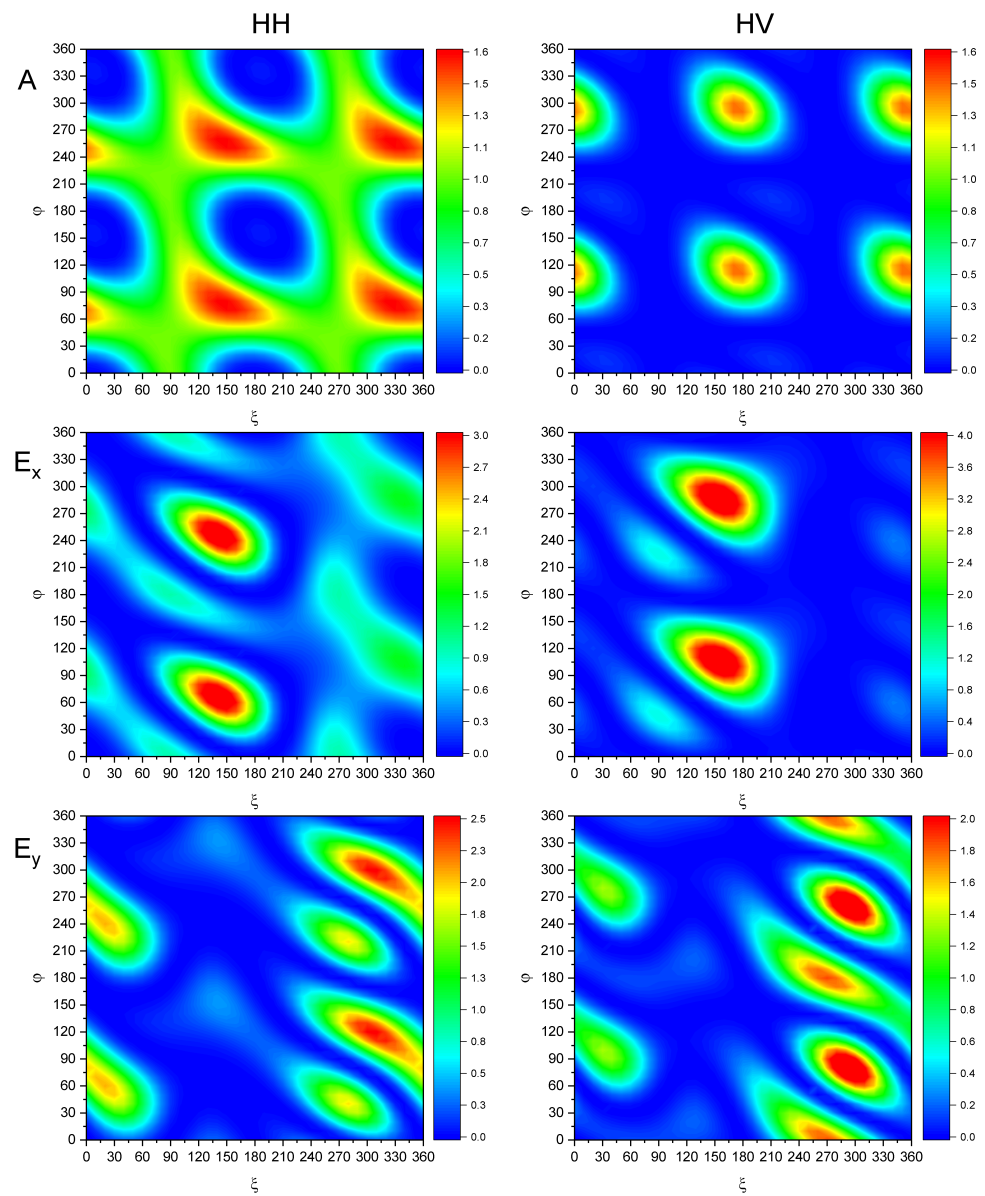


Figure A4. Rotation angle intensity map of calculated Raman modes in HH and HV polarisation.

$$\Phi_{xyz} = \begin{pmatrix} \cos(\alpha) \cos(\gamma) - \sin(\alpha) \cos(\beta) \sin(\gamma) & \sin(\alpha)(-\cos(\gamma)) - \cos(\alpha) \cos(\beta) \sin(\gamma) & \sin(\beta) \sin(\gamma) \\ \sin(\alpha) \cos(\beta) \cos(\gamma) + \cos(\alpha) \sin(\gamma) & \cos(\alpha) \cos(\beta) \cos(\gamma) - \sin(\alpha) \sin(\gamma) & \sin(\beta)(-\cos(\gamma)) \\ \sin(\alpha) \sin(\beta) & \cos(\alpha) \sin(\beta) & \cos(\beta) \end{pmatrix} \quad (\text{A1})$$

$$I_{A_1}^{\parallel} \propto [a(\sin(\alpha) \cos(\beta) \cos(\gamma) + \cos(\alpha) \sin(\gamma))^2 + a(\cos(\alpha) \cos(\beta) \cos(\gamma) - \sin(\alpha) \sin(\gamma))^2 + b \sin^2(\beta) \cos^2(\gamma)]^2 \quad (\text{A2})$$

$$I_{A_1}^{\perp} = (a - b)^2 \sin^4(\beta) \sin^2(\gamma) \cos^2(\gamma) \quad (\text{A3})$$

$$I_{E_x}^{\parallel} \propto [c \cos^2(\alpha) (\sin^2(\gamma) - \cos^2(\beta) \cos^2(\gamma)) + \sin(\alpha) (c \sin(\alpha) \cos^2(\beta) \cos^2(\gamma) - c \sin(\alpha) \sin^2(\gamma) + d \sin(\beta) \sin(2\gamma)) - 2 \cos(\alpha) \cos(\beta) \cos(\gamma) (d \sin(\beta) \cos(\gamma) - 2c \sin(\alpha) \sin(\gamma))]^2 \quad (\text{A4})$$

$$I_{E_x}^{\perp} \propto [c(\sin(\alpha) \cos(\beta) \cos(\gamma) + \cos(\alpha) \sin(\gamma))(\cos(\alpha) \cos(\gamma) - \sin(\alpha) \cos(\beta) \sin(\gamma)) + (\cos(\alpha) \cos(\beta) \sin(\gamma) + \sin(\alpha) \cos(\gamma))(c \cos(\alpha) \cos(\beta) \cos(\gamma) - c \sin(\alpha) \sin(\gamma) + d \sin(\beta) \cos(\gamma)) + d \sin(\beta) \sin(\gamma)(\cos(\alpha) \cos(\beta) \cos(\gamma) - \sin(\alpha) \sin(\gamma))]^2 \quad (A5)$$

$$I_{E_y}^{\parallel} \propto 4[\sin(\alpha) \cos(\beta) \cos(\gamma) + \cos(\alpha) \sin(\gamma)]^2(-c \cos(\alpha) \cos(\beta) \cos(\gamma) + c \sin(\alpha) \sin(\gamma) + d \sin(\beta) \cos(\gamma))^2 \quad (A6)$$

$$I_{E_y}^{\perp} = [c(\cos(\alpha) \cos(\beta) \sin(\gamma) + \sin(\alpha) \cos(\gamma))(\sin(\alpha) \cos(\beta) \cos(\gamma) + \cos(\alpha) \sin(\gamma)) + (\cos(\alpha) \cos(\gamma) - \sin(\alpha) \cos(\beta) \sin(\gamma))(-c \cos(\alpha) \cos(\beta) \cos(\gamma) + c \sin(\alpha) \sin(\gamma) + d \sin(\beta) \cos(\gamma)) - d \sin(\beta) \sin(\gamma)(\sin(\alpha) \cos(\beta) \cos(\gamma) + \cos(\alpha) \sin(\gamma))]^2 \quad (A7)$$

Appendix B. Photos of the $\text{TbFe}_{2.46}\text{Ga}_{0.54}(\text{BO}_3)_4$ Crystal in the DAC

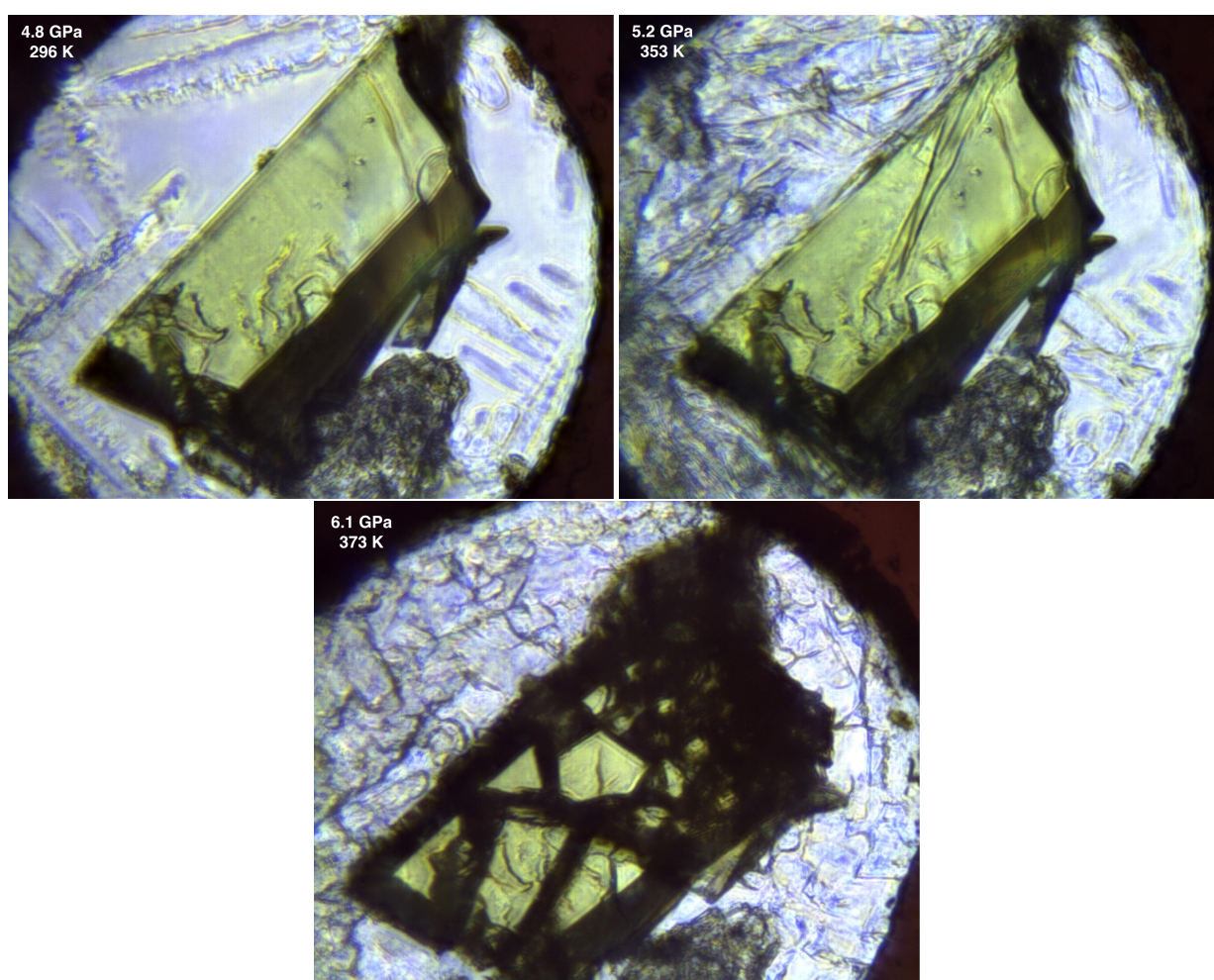


Figure A5. Sample and high-pressure sensor in the high-pressure diamond anvil cell (DAC) at different pressure–temperature conditions; 4:1 methanol–ethanol alcohol mixture as a pressure transmitting media.

References

1. Vopson, M.M. Fundamentals of Multiferroic Materials and Their Possible Applications. *Crit. Rev. Solid State Mater. Sci.* **2015**, *40*, 223–250. [[CrossRef](#)]
2. Fiebig, M. Revival of the magnetoelectric effect. *J. Phys. D Appl. Phys.* **2005**, *38*, R123–R152. [[CrossRef](#)]
3. Eerenstein, W.; Mathur, N.D.; Scott, J.F. Multiferroic and magnetoelectric materials. *Nature* **2006**, *442*, 759–765. [[CrossRef](#)] [[PubMed](#)]

4. Hinatsu, Y.; Doi, Y.; Ito, K.; Wakeshima, M.; Alemi, A. Magnetic and calorimetric studies on rare-earth iron borates $\text{LnFe}_3(\text{BO}_3)_4$ ($\text{Ln} = \text{Y}, \text{La-Nd}, \text{Sm-Ho}$). *J. Solid State Chem.* **2003**, *172*, 438–445. [\[CrossRef\]](#)
5. Krylov, A.S.; Sofronova, S.N.; Gudim, I.A.; Vtyurin, A.N. Magnetoelastic interactions in Raman spectra of $\text{Ho}_{1-x}\text{Nd}_x\text{Fe}_3(\text{BO}_3)_4$ crystals. *Solid State Commun.* **2013**, *174*, 26–29. [\[CrossRef\]](#)
6. Krylov, A.S.; Sofronova, S.N.; Gudim, I.A.; Krylova, S.N.; Kumar, R.; Vtyurin, A.N. Manifestation of magnetoelastic interactions in Raman spectra of $\text{Ho}_x\text{Nd}_{1-x}\text{Fe}_3(\text{BO}_3)_4$ crystals. *J. Adv. Dielectr.* **2018**, *8*, 1850011. [\[CrossRef\]](#)
7. Leonyuk, N.I.; Leonyuk, L.I. Growth and characterization of $\text{RM}_3(\text{BO}_3)_4$ crystals. *Prog. Cryst. Growth. Charact.* **1995**, *31*, 179–278. [\[CrossRef\]](#)
8. Moshkina, E.; Krylov, A.; Sofronova, S.; Gudim, I.; Temerov, V. Crystal Growth and Raman Spectroscopy Study of $\text{Sm}_{1-x}\text{La}_x\text{Fe}_3(\text{BO}_3)_4$ Ferroborates. *Cryst. Growth Des.* **2016**, *16*, 6915–6921. [\[CrossRef\]](#)
9. Moshkina, E.; Krylova, S.; Gudim, I.; Molokeev, M.; Temerov, V.; Pavlovskiy, M.S.; Vtyurin, A.; Krylov, A. Gallium Composition-Dependent Structural Phase Transitions in $\text{HoFe}_{3-x}\text{Ga}_x(\text{BO}_3)_4$ Solid Solutions: Crystal Growth, Structure, and Raman Spectroscopy Study. *Cryst. Growth Des.* **2020**, *20*, 1058–1069. [\[CrossRef\]](#)
10. Fausti, D.; Nugroho, A.A.; van Loosdrecht, P.H.; Klimin, S.A.; Popova, M.N.; Bezmaternykh, L.N. Raman scattering from phonons and magnons in $\text{RFe}_3(\text{BO}_3)_4$. *Phys. Rev. B* **2006**, *74*, 024403. [\[CrossRef\]](#)
11. Ritter, C.; Balaev, A.; Vorotynov, A.; Petrakovskii, G.; Velikanov, D.; Temerov, V.; Gudim, I. Magnetic structure, magnetic interactions and metamagnetism in terbium iron borate $\text{TbFe}_3(\text{BO}_3)_4$: A neutron diffraction and magnetization study. *J. Phys. Condens. Matter* **2007**, *19*, 196227. [\[CrossRef\]](#)
12. Popova, E.A.; Volkov, D.V.; Vasiliev, A.N.; Demidov, A.A.; Kolmakova, N.P.; Gudim, I.A.; Bezmaternykh, L.N.; Tristan, N.; Skourski, Y.; Büchner, B.; et al. Magnetization and specific heat of $\text{TbFe}_3(\text{BO}_3)_4$: Experiment and crystal-field calculations. *Phys. Rev. B* **2007**, *75*, 224413. [\[CrossRef\]](#)
13. Pavlovskiy, M.S.; Shaykhutdinov, K.A.; Wu, L.S.; Ehlers, G.; Temerov, V.L.; I. A. Gudim, A.S.S.; Podlesnyak, A. Observation of soft phonon mode in $\text{TbFe}_3(\text{BO}_3)_4$ by inelastic neutron scattering. *Phys. Rev. B* **2018**, *97*, 054313. [\[CrossRef\]](#)
14. Volkov, D.V.; Popova, E.A.; Kolmakov, N.P.; Demidov, A.A.; Tristan, N.; Skourski, Y.; Buechner, B.; Gudim, I.A.; Bezmaternykh, L.N. Magnetic properties of $\text{TbFe}_3(\text{BO}_3)_4$. *JMMM* **2007**, *316*, e717–e720. [\[CrossRef\]](#)
15. Stanislavchuk, T.N.; Chukalina, E.P.; Bezmaternykh, L.N. Study of magnetic phase transitions and magnetic structures in a number of rare-earth ferroborates using an erbium spectroscopic probe. *J. Opt. Technol.* **2007**, *74*, 139–143. [\[CrossRef\]](#)
16. Gnatchenko, S.L.; Kachur, I.S.; Piryatinskaya, V.G.; Bedarev, V.A.; Pashchenko, M.I. Spectroscopic and magneto-optical investigations of spin-reorientation phase transition in $\text{TbFe}_3(\text{BO}_3)_4$. *Low Temp. Phys.* **2011**, *37*, 693–698. [\[CrossRef\]](#)
17. Szaller, D.; Kocsis, V.; Bordács, S.; Fehér, T.; Rőöm, T.; Nagel, U.; Engelkamp, H.; Ohgushi, K.; Kézsmárki, I. Magnetic resonances of multiferroic $\text{TbFe}_3(\text{BO}_3)_4$. *Phys. Rev. B* **2017**, *95*, 024427. [\[CrossRef\]](#)
18. Krylova, S.; Gudim, I.; Aleksandrovsky, A.; Vtyurin, A.; Krylov, A. Electronic band structures of $\text{NdFe}_3(\text{BO}_3)_4$ and $\text{NdGa}_3(\text{BO}_3)_4$ crystals: ab initio calculations. *Ferroelectrics* **2021**, *575*, 11–17. [\[CrossRef\]](#)
19. Krylova, S.N.; Aleksandrovsky, A.S.; Roginskii, E.M.; Krylov, A.A.; Gudim, I.A.; Vtyurin, A.N. Optical properties of the $\text{HoGa}_3(\text{BO}_3)_4$ crystal: experiment and ab initio calculation. *Ferroelectrics* **2020**, *559*, 135–140. [\[CrossRef\]](#)
20. Klimin, S.A.; Fausti, D.; Meetsma, A.; L. N. Bezmaternykh, c.P.H.M.v.L.; Palstra, T.T.M. Evidence for differentiation in the iron-helical chain in $\text{GdFe}_3(\text{BO}_3)_4$. *Acta Cryst. B* **2005**, *61*, 481–485. [\[CrossRef\]](#)
21. Krylov, A.S.; Gudim, I.A.; Krylova, S.N.; Krylov, A.A.; Vtyurin, A.N. Structural phase transition in $\text{TbFe}_{2.5}\text{Ga}_{0.5}(\text{BO}_3)_4$ single crystal. *Ferroelectrics* **2020**, *559*, 128–134. [\[CrossRef\]](#)
22. Moshkina, E.; Gudim, I.; Temerov, V.; Krylov, A. Temperature-dependent absorption lines observation in Raman spectra of $\text{SmFe}_3(\text{BO}_3)_4$ ferroborate. *J. Raman Spectrosc.* **2018**, *49*, 1732–1735. [\[CrossRef\]](#)
23. Popova, M.N.; Stanislavchuk, T.N.; Malkin, B.Z.; Bezmaternykh, L.N. Phase transitions and crystal-field and exchange interactions in $\text{TbFe}_3(\text{BO}_3)_4$ as seen via optical spectroscopy. *J. Phys. Condens. Matter* **2012**, *24*, 196002. [\[CrossRef\]](#)
24. Peschanskii, A.V.; Yermenko, A.V.; Fomin, V.I.; Bezmaternykh, L.N.; Gudim, I.A. Raman scattering under structural and magnetic phase transitions in terbium ferroborate. *Low Temp. Phys.* **2014**, *40*, 171–178. [\[CrossRef\]](#)
25. Adem, U.; Wang, L.; Fausti, D.; Schottenhamel, W.; van Loosdrecht, P.H.M.; Vasiliev, A.; Bezmaternykh, L.N.; Büchner, B.; Hess, C.; Klingeler, R. Magnetodielectric and magnetoelastic coupling in $\text{TbFe}_3(\text{BO}_3)_4$. *Phys. Rev. B* **2010**, *82*, 064406. [\[CrossRef\]](#)
26. Bedarev, V.; Pashchenko, M.; Merenkov, D.; Savina, Y.; Pashchenko, V.; Gnatchenko, S.; Bezmaternykh, L.; Temerov, V. The Faraday effect in $\text{TbFe}_3(\text{BO}_3)_4$ and $\text{TbAl}_3(\text{BO}_3)_4$ borates. *J. Magnet. Magnet. Mater.* **2014**, *362*, 150–153. [\[CrossRef\]](#)
27. Krylov, A.S.; Gudim, I.A.; Nemtsev, I.; Krylova, S.N.; Shabanov, A.V.; Krylov, A.A. Raman study of $\text{HoFe}_3(\text{BO}_3)_4$ at simultaneously high pressure and high temperature: p–T phase diagram. *J. Raman Spectrosc.* **2017**, *48*, 1406–1410. [\[CrossRef\]](#)
28. Krylov, A.; Pavlovskiy, M.; Kitaev, Y.; Gudim, I.; Andryshin, N.; Vtyurin, A.; Jiang, Q.; Krylova, S. Phase transitions and p–T phase diagram of the multiferroic $\text{TbFe}_3(\text{BO}_3)_4$ crystal. *J. Raman Spectrosc.* **2022**. [\[CrossRef\]](#)
29. Datchi, F.; Dewaele, A.; Loubeyre, P.; Letoullec, R.; Godec, Y.L.; Canny, B. Optical pressure sensors for high-pressure–high-temperature studies in a diamond anvil cell. *High Press. Res.* **2007**, *27*, 447–463. [\[CrossRef\]](#)
30. Rashchenko, S.V.; Kurnosov, A.; Dubrovinsky, L.; Litasov, K.D. Revised calibration of the $\text{Sm}:\text{SrB}_4\text{O}_7$ pressure sensor using the Sm-doped yttrium-aluminum garnet primary pressure scale. *J. Appl. Phys.* **2015**, *117*, 145902. [\[CrossRef\]](#)
31. Orobengoa, D.; Capillas, C.; Aroyo, M.I.; Perez-Mato, J.M. AMPLIMODES: symmetry-mode analysis on the Bilbao Crystallographic Server. *J. Appl. Crystallogr.* **2009**, *42*, 820–833. [\[CrossRef\]](#)

32. Perez-Mato, J.M.; Orobengoa, D.; Aroyo, M.I. Mode crystallography of distorted structures. *Acta Crystallogr. Sect. A* **2010**, *66*, 558–590. [[CrossRef](#)]
33. Choi, Y.; Kim, K.; Lim, S.Y.; Kim, J.; Park, J.M.; Kim, J.H.; Lee, Z.; Cheong, H. Complete determination of the crystallographic orientation of ReX₂ (X = S, Se) by polarized Raman spectroscopy. *Nanoscale Horiz.* **2020**, *5*, 308–315. [[CrossRef](#)]
34. Peticolas, W.L.; Nafie, L.; Stein, P.; Fanconi, B. Quantum Theory of the Intensities of Molecular Vibrational Spectra. *J. Chem. Phys.* **1970**, *52*, 1576–1584. [[CrossRef](#)]
35. Chang, Y.; He, S.; Sun, M.; Xiao, A.; Zhao, J.; Ma, L.; Qiu, W. Angle-Resolved Intensity of In-Axis/Off-Axis Polarized Micro-Raman Spectroscopy for Monocrystalline Silicon. *J. Spectrosc.* **2021**, p. 2860007. [[CrossRef](#)]
36. Aroyo, M.I. (Ed.) *International Tables for Crystallography. Vol. A. Space Group Symmetry*, 6th ed.; Wiley: Hoboken, NJ, USA, 2016.
37. Litvin, D.B. Magnetic space-group types. *Acta Crystallogr. Sect. A* **2001**, *57*, 729–730. [[CrossRef](#)]
38. Wills, A.. Magnetic structures and their determination using group theory. *J. Phys. IV France* **2001**, *11*, Pr9–133–Pr9–158. [[CrossRef](#)]
39. Litvin, D. *Magnetic Group Tables: 1-, 2-, and 3-Dimensional Magnetic Subperiodic Groups and Magnetic Space Groups*; International Union of Crystallography: Chester, UK, 2013. [[CrossRef](#)]
40. Cracknell, A.P. Space-Group Selection Rules for Magnetic Crystals. *Prog. Theoret. Phys.* **1967**, *38*, 1252–1269. [[CrossRef](#)]
41. Shubnikov, A.V.; Belov, N. *Colored Symmetry*, 6th ed.; Pergamon Press: Oxford, UK, 1964.
42. Krylov, A.; Vtyurin, A.; Gudim, I.; Nemtsev, I.; Krylova, S. Phase diagram and soft modes behaviour TbFe_{3–x}GaX(BO₃)₄ solid solutions with huntite structures. *Opt. Spectrosc.* **2022**, *130*, 84–91.
43. Salje, E.K.; Bismayer, U. Hard mode spectroscopy: The concept and applications. *Phase Transit.* **1997**, *63*, 1–75. [[CrossRef](#)]
44. Bismayer, U. Hard Mode Spectroscopy of Phase Transitions. *Rev. Mineral. Geochem.* **2000**, *39*, 265–283. [[CrossRef](#)]
45. Bismayer, U. Hard mode Raman spectroscopy and its application to ferroelastic and ferroelectric phase transitions. *Phase Transit.* **1990**, *27*, 211–267. [[CrossRef](#)]
46. Salje, E.K.H. Hard mode Spectroscopy: Experimental studies of structural phase transitions. *Phase Transit.* **1992**, *37*, 83–110. [[CrossRef](#)]
47. Piermarini, G.J.; Block, S.; Barnett, J.D.; Forman, R.A. Calibration of the pressure dependence of the R1 ruby fluorescence line to 195 kbar. *J. Appl. Phys.* **1975**, *46*, 2774–2780. [[CrossRef](#)]
48. Ragan, D.D.; Gustavsen, R.; Schiferl, D. Calibration of the ruby R1 and R2 fluorescence shifts as a function of temperature from 0 to 600 K. *J. Appl. Phys.* **1992**, *72*, 5539–5544. [[CrossRef](#)]